

LETTER TO THE EDITOR

Mare versus highland lunar impact flash light curve dichotomy

D. Athanasopoulos¹*, A. Liakos¹, A. Z. Bonanos¹, D. Koschny², O. Sykioti¹, M. Devogèle³, J. L. Cano⁵, and R. Moissl⁵

¹ IAASARS, National Observatory of Athens, 15236 Penteli, Greece

² Technical University of Munich, Lunar and Planetary Exploration, Lise-Meitner-Str. 9, 85521 Ottobrunn, Germany

³ ESA NEO Coordination Centre, European Space Agency, Largo Galileo Galilei, 1, 00044, Frascati, RM, Italy

⁴ ESA ESOC, Planetary Defence Office, Robert-Bosch-Strasse 5, 64293 Darmstadt, Germany

Received May 17, 2026

ABSTRACT

We perform a comprehensive analysis of lunar impact flash (LIF) light curve shapes and their dependence on the lunar terrain, using the large sample of LIFs detected by NELIOTA over the last 9 years. We classified 124 multi-frame light curves into mare, highland and ‘border’ regions. Subsequently, we derived analytical expressions for single-size and dual-size ejecta cooling models, which were fitted to the observational data to estimate their physical properties. While impacts on both terrains yield similar peak magnitude distributions, their decay behaviour differs significantly; highland LIFs exhibit a shallower and longer-lasting decay ($\tau = 0.11^{+0.08}_{-0.05}$ s) compared to mare flashes, which are faster and steeper ($\tau = 0.038^{+0.032}_{-0.018}$ s). The dual-size model suggests this extended duration is primarily driven by the fine droplets of the ejecta. The profile and duration of the LIF light curves represent the initial stages of the impact cratering process. The observed dichotomy between highland and mare LIFs demonstrates that the initial stages of the impact cratering process are fundamentally dependent on lunar lithology.

Key words. Moon – Meteoroids – Impact phenomena – Techniques: photometric – Planets and satellites: surfaces

1. Introduction

Hypervelocity impacts are among the most energetic processes in the Solar System, yet the physics of the initial cratering process remains inaccessible to laboratory replication. The Moon serves as a premier natural laboratory where meteoroid strikes occur at speeds far exceeding experimental limits. On airless bodies, impacts of meteoroids produce luminous transient events in the visible and near-infrared during the initial stages of the cratering process. Photons are produced by the partial conversion of the impactor’s kinetic energy into thermal radiation governed by the critical parameter known as luminous efficiency (Bouley et al. 2012). While lunar surface lithology is known to shape late-stage crater morphology, its influence on the initial stages of impact and the resulting lunar impact flashes (LIFs) has remained elusive.

While unverified reports of such phenomena have existed for centuries (Kolovos et al. 1988, and references therein), the modern era of lunar impact monitoring began with the 1999 Leonid meteor stream (Ortiz et al. 2000; Artem’eva et al. 2001; Yanagisawa & Kisaichi 2002; Cudnik et al. 2003b). Since then, many observing campaigns have been performed (e.g., Ortiz et al. 2002, 2006, 2015; Cudnik et al. 2003a; Yanagisawa et al. 2006, 2021, 2025; Suggs et al. 2008, 2014; Ait Moulay Larbi et al. 2015; Bonanos et al. 2018; Madiedo et al. 2018, 2019; Liakos et al. 2020, 2024; Sheward et al. 2024), transforming the Moon into a natural laboratory for hypervelocity impact physics.

Studies of impact craters on the Earth and the Moon have demonstrated that the target composition, specifically the lithol-

ogy, plays a significant role in the impact cratering process (see, Osinski et al. 2019, and references therein). However, no equivalent study has examined its potential effect on LIF properties. The lunar surface is morphologically heterogeneous: the high albedo regions (i.e. highlands) represent the primary lunar crust, whereas the low-albedo maria are basaltic plains formed by subsequent volcanism, exhibiting vastly different mineralogy (e.g., Borg & Carlson 2023). In this study, we leverage the large LIF sample produced by the NELIOTA programme (Xilouris et al. 2018; Bonanos et al. 2018; Liakos et al. 2020, 2024) to examine the dependency of LIF light curve behaviour on the lunar terrain.

2. Multi-frame lunar impact flashes

2.1. Datasets

To date, NELIOTA¹ has produced the largest publicly available LIF dataset, consisting of 329 reported LIFs (Liakos et al. 2020, 2024, and herein). At least 50% of the total sample comprise at least two measurements in the *I* filter; these are referred to as ‘multi-frame’ events with a minimum duration of 66 ms, while events exceeding 100 ms are hereafter termed ‘long’ events. The majority of LIFs (~75%) have not been associated with known meteoroid streams and are called ‘sporadics’, expected to be chondrites, similar to most common meteorites (Brož et al. 2024).

We include 109 archival NELIOTA multi-frame LIFs documented in Liakos et al. (2020, 2024) and classified as sporadic; these provide a robust sample with randomised impact velocity, averaging 24 km s⁻¹ (Suggs et al. 2014), thereby isolating the

* Corresponding author: dimathanaso@noa.gr

¹ neliota.astro.noa.gr

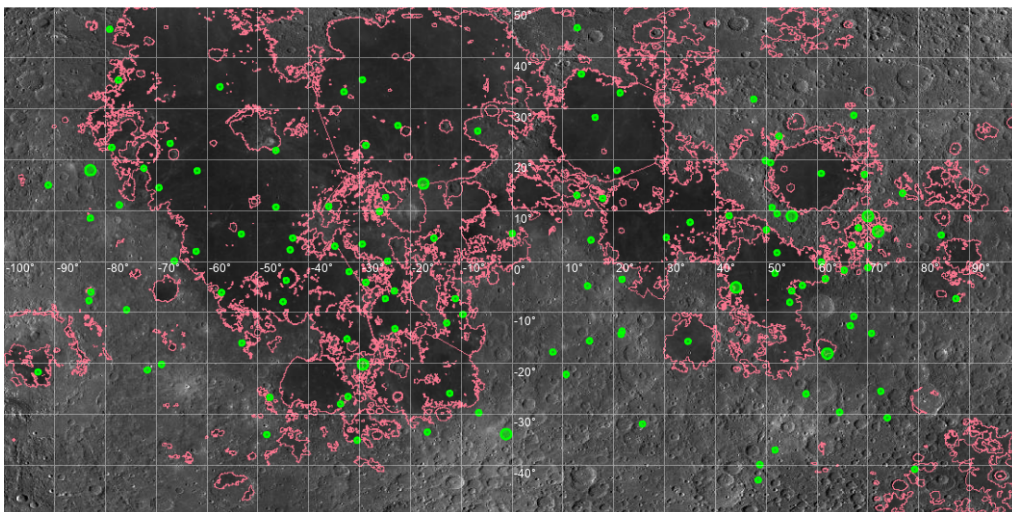


Fig. 1: NELIOTA multi-frame LIF sample (green ellipses, scaled according to their localisation accuracy) superimposed on a lunar map of the near side. Mare boundaries are highlighted by solid magenta lines.

influence of the target terrain on the resulting flash. This dataset has been further enriched by 34 LIF detections recorded between August 2025 and February 2026 (Table A.1) of which 15 were identified as sporadic multi-frame LIFs and included in our analysis (Table A.2). In total, our sample consists of 124 multi-frame LIFs, of which 97 have been validated (see Table A.3). Figure 1 presents a visualisation of the spatial distribution of the LIF sample on a lunar map mosaic generated by Wagner et al. (2015).

2.2. Terrain classification of the LIF locations

We adopted the grouping scheme of Osinski et al. (2019) to classify the LIF sample according to the terrain type of their detected locations: mare, highland, and ‘border’. For this classification, the mare boundaries defined by Nelson et al. (2014) were used (see Fig. 1); a mare or highland event is defined as one where the LIF localisation area, including its associated uncertainty, overlaps a mare or highland region by at least 95%, respectively. Conversely, ‘border’ LIFs are those occurring near the interface between mare and highland terrains, where the localisation area overlaps the mare boundaries by between 5% and 95% (Table A.4). Figure 2 presents the distribution of the LIF durations, grouped by terrain type.

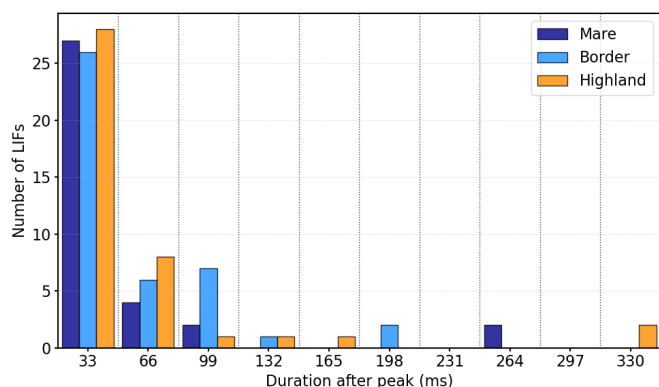


Fig. 2: Distribution of multi-frame sporadic LIFs versus their duration and grouped by terrain type.

2.3. Photometry and light curve normalisation

We performed aperture photometry for the newly detected LIFs, following the methodology described by Liakos et al. (2020) and we applied a two-step normalisation process. The first step consisted of a temporal shift, wherein we aligned all peak magnitudes to a relative temporal origin designated as ‘Frame 1’ (at $t_0 = 0$ s). Measurements prior to the peak were matched to ‘Frame 0’. The second step involved the normalisation of the peak amplitudes by setting the peak relative magnitude value to zero, which intrinsically corresponds to a maximum normalised flux of 1. This resulting dimensionless representation is paramount for systematically evaluating the characteristic cooling rates, durations, and decay behaviours of sporadic LIFs detected on different lunar terrain types.

3. Ejecta cooling models

The maximum luminosity of a LIF (i.e. the light curve peak) is primarily attributed to a vapour cloud or plasma radiation (Bouley et al. 2012; Yanagisawa et al. 2025). Laboratory experiments have demonstrated that the radiation emitted by the vapour cloud lasts less than 1 ms (Gores & Spray 2022). The post-peak emission is expected to originate from the ejecta material, extending the total flash duration from 10 ms up to 1 s for events within the 4–10 peak magnitude range (Bouley et al. 2012).

In this work, we derived analytical expressions for the ejecta cooling models of Yanagisawa & Kisaichi (2002) and Yanagisawa et al. (2025), adapting the mathematical formalism provided by Bouley et al. (2012). Notably, we depart from the use of the Stefan-Boltzmann law, as it represents the integrated flux over the entire spectrum; instead, we account for the band-specific response of photometric filters. Further details are provided in Appendix B.

The absolute observed flux is described by:

$$F_{\lambda}(t) = F_{\lambda,0} \cdot \Phi(t), \quad (1)$$

where $F_{\lambda,0}$ is the initial flux of the droplet model, starting after the peak at reference time (t_{ref}) and $\Phi(t)$ is the light curve decay function defined as:

$$\Phi(t) = \left[e^{\frac{hc}{\lambda_{\text{eff}} k_B T_0} \left(1 + \frac{t - t_{\text{ref}}}{\tau}\right)^{1/3}} - 1 \right]^{-1}, \quad (2)$$

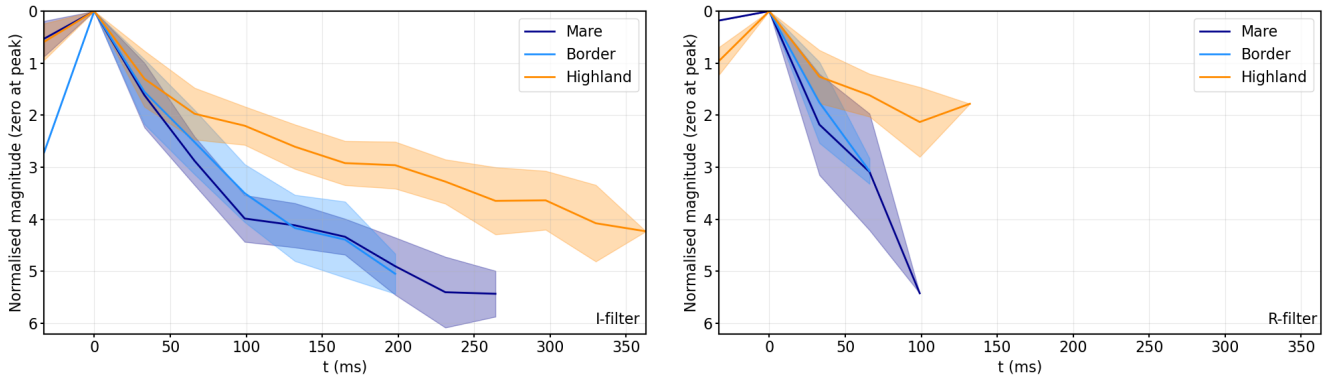


Fig. 3: Average LIF light curves (including rms) for each terrain type in the *I*-filter (left panel) and *R*-filter (right panel).

where h is Planck’s constant, c is the speed of light, λ_{eff} is the effective wavelength of the filter, k_B is the Boltzmann constant, T_0 is the initial temperature of the droplet model at time t_{ref} , and τ is the characteristic cooling timescale, as defined in Appendix B.

The normalised flux can be described by the following equation in the single-size model:

$$F_{\text{norm}}(t) = F_{\text{ref}} \cdot \frac{\Phi(t)}{\Phi(t_{\text{ref}})} + C_{\text{bg}}, \quad (3)$$

where $F_{\text{ref}} = \frac{F_A(t_{\text{ref}})}{F_{\text{peak}}}$ represents the fractional amplitude ($0 \leq F_{\text{ref}} \leq 1$) of the data at the onset of the molten droplet phase. Additionally, C_{bg} is a mathematical baseline offset intended to account for non-zero instrumental noise. The shape of this normalised thermal tail depends entirely on F_{ref} , T_0 , and τ .

Yanagisawa et al. (2025) suggested that two distinct particle populations are ejected during the excavation phase, both of which contribute to the LIF radiation. Initially, fine molten droplets form at temperatures near the vaporisation point of lunar minerals, followed by the ejection of coarse particles at lower initial temperatures. Due to their larger volume-to-surface-area ratio, these coarse particles cool much more slowly, acting as the primary source of the sustained afterglow.

Following the same mathematical derivation as for the single-size model, Eq. (3) is expanded to account for both the fine (f) and coarse (c) populations:

$$F_{\text{norm}}(t) = F_{\text{ref}} \cdot \frac{\Phi_f(t) + A_R \Phi_c(t)}{\Phi_f(t_{\text{ref}}) + A_R \Phi_c(t_{\text{ref}})} + C_{\text{bg}}, \quad (4)$$

where A_R is the cross-sectional area ratio between the coarse and fine particles.

In this work, we did not consider explicit regolith properties as fixed inputs. Instead, we employed a Markov Chain Monte Carlo (MCMC) approach applied exclusively to the *I*-filter average LIF light curve (due to its extended duration compared to the *R*-filter) to explore the range of physical parameters in the analytical expressions (Eqs. 3 & 4) that could explain the observational data (see Appendix C for details).

4. Results and discussion

We plot the average normalised light curves grouped by terrain type and find that they exhibit distinct morphologies (Fig. 3). A dichotomy between mare and highland LIFs becomes apparent approximately 50 ms after the peak. Highland LIFs display a slower decay than mare and ‘border’ flashes, which show similar

behaviour. The dichotomy also persists when considering only validated LIFs, with the root mean square (rms) values being consistent with the full sample.

The magnitude offset between the afterglow light curves is a result of the apparent peak magnitude difference between mare and highland long LIFs, with the former appearing ~ 1.2 mag fainter than the latter. While the general distribution of apparent peak magnitudes is similar for each group, their initial magnitude decay differs significantly; mare and ‘border’ LIFs exhibit an initial drop approximately twice as large as that observed for highland events (Fig. A.1), indicating that the dichotomy is not solely a result of the long, bright, LIFs. Furthermore, for a given peak magnitude, highland LIFs exhibit longer durations than their mare counterparts (Fig. A.2).

The extended duration and slower decay of highland LIFs can result in up to 30% higher luminous energy compared to a mare LIF of the same peak magnitude. If the impactor’s kinetic energy is directly linked to the peak magnitude, then luminous efficiency will also be terrain-dependent, rather than solely a function of impactor velocity as suggested by Swift et al. (2011) and Fuse et al. (2020). However, the divergent observed light curves suggest a difference in initial energy partitioning. Mare LIFs, which feature a rapid magnitude drop, may lose a significant fraction of energy to the crushing and compaction of the denser basaltic target. Conversely, a highland LIF of equivalent energy may produce a fainter peak but more persistent emission, as the impact energy is absorbed by the porous highland regolith, facilitating a more gradual thermal release.

The MCMC fitting of the single-size and dual-size thermal models on the NELIOTA data (Fig. 4) uses the analytical expressions from Eqs. (3) and (4), respectively. The final optimised parameters are summarised in Table C.1. When the single-size model is applied, the solutions for both mare and highland LIFs yield a comparable reference temperature of ~ 3000 K. However, they exhibit distinct cooling timescales: $\tau = 38^{+32}_{-18}$ ms for the maria and notably longer ($\tau = 110^{+80}_{-50}$ ms) for the highlands. The dual-size model predicts a stronger afterglow. For the fine droplet component, both terrains exhibit similar reference temperatures in the range $3600 - 3700$ K, yet their cooling timescales differ slightly: $\tau_f = 25^{+14}_{-11}$ ms for the maria compared to $\tau_f = 36^{+10}_{-13}$ ms for the highlands. In contrast, the coarse particle component demonstrates disparate reference temperatures: $T_c = 2200^{+600}_{-500}$ K for the maria and $T_c = 2700^{+500}_{-600}$ K for the highlands, while sharing an identical, extended cooling timescale of $\tau_c = 0.5^{+0.3}_{-0.3}$ s across both terrain types. Notably, the reference temperatures for both models are lower than 3800 K, which is

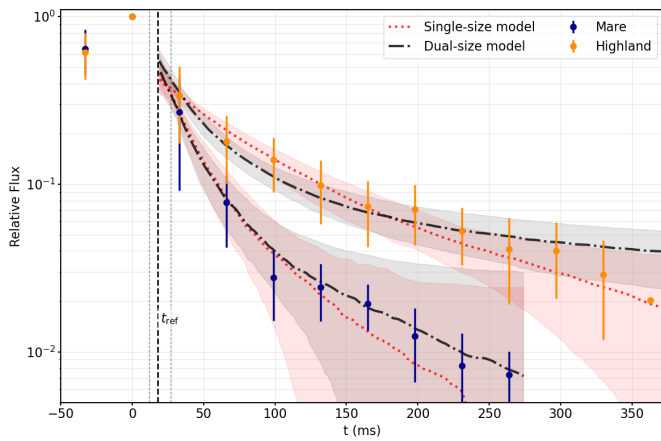


Fig. 4: Best fit MCMC ejecta cooling models on the average (mare and highland) light curves (see Appendix C for details).

the estimated vaporisation temperature of the lunar regolith reported in previous studies (Cintala 1992, and references therein).

5. Conclusions

We analysed a sample of 124 multi-frame sporadic LIFs detected by NELIOTA and identified a dichotomy in their light-curve behaviour as a function of terrain type. LIFs occurring on the highlands exhibit shallower and longer decay than those on the maria. ‘Border’ LIFs display faster, steeper decay profiles similar to those of mare LIFs. The light curves were fitted using the newly derived analytical expressions based on the models of Yanagisawa & Kisaichi (2002) and Yanagisawa et al. (2025), which quantifying the initial temperatures and characteristic timescales for each terrain type. These expressions can be used to estimate the total luminous energy from location and temperature evolution using only a single band.

While studies so far have focused on the influence of surface lithology on late-stage crater morphology, this work provides the first evidence that lunar terrain also plays a significant role in initial energy partitioning during the earliest stages of the cratering process. The rapid magnitude drop observed in mare LIFs may be attributed to the denser basaltic target, where a significant fraction of the impact energy is consumed by the crushing and compaction of the consolidated rock. Conversely, the porous regolith of the highlands may facilitate a more gradual energy release, resulting in the persistent thermal tails observed in our sample. Whether these results indicate a fundamentally terrain-dependent luminous efficiency remains an open question. Analogous studies focusing on major meteoroid streams will be critical in providing an answer; in such cases, the impactor velocity and composition, parameters that also influence initial temperature (Rakesh Chandra 2026), are more strictly constrained, allowing the influence of target lithology to be isolated.

The current study will serve as a highly valuable framework for the forthcoming Lunar Meteoroid Impacts Observer (LUMIO) CubeSat mission (Ferrari et al. 2025) of ESA, which will monitor the far side of the Moon for one year. Given that the far side is dominated by highlands, our results imply LUMIO will detect more long LIFs. Future work will investigate correlations between surface parameters and observed fluxes, alongside temperature estimations derived via the $R-I$ colour index with the NELIOTA system (Bonanos et al. 2018; Avdellidou & Vaubaillon 2019; Liakos et al. 2020).

Acknowledgements. This work has made use of data from the NELIOTA project funded by the ESA. This study is based on observations made with the 1.2 m Kryoneri telescope, Corinthia, Greece, which is operated by the IAASARS, NOA. DA gratefully acknowledges financial support by the Horizon Europe Programme of the EU implemented by ESA under the NELIOTA-III programme, contract No. 4000148793/25/D/MRP. Views and opinion expressed are however those of the authors only and the European Commission cannot be held responsible for any use which may be made of the information contained therein.

References

- Ait Moulay Larbi, M., Daassou, A., Baratoux, D., et al. 2015, *Earth Moon and Planets*, 115, 1
- Artem’eva, N. A., Kosarev, I. B., Nemtchinov, I. V., Trubetskaya, I. A., & Shuvalov, V. V. 2001, *Solar System Research*, 35, 177
- Avdellidou, C. & Vaubaillon, J. 2019, *MNRAS*, 484, 5212
- Bonanos, A. Z., Avdellidou, C., Liakos, A., et al. 2018, *A&A*, 612, A76
- Borg, L. E. & Carlson, R. W. 2023, *Annual Review of Earth and Planetary Sciences*, 51, 25
- Bouley, S., Baratoux, D., Vaubaillon, J., et al. 2012, *Icarus*, 218, 115
- Brož, M., Vernazza, P., Marsset, M., et al. 2024, *Nature*, 634, 566
- Cintala, M. J. 1992, *J. Geophys. Res.*, 97, 947
- Cudnik, B. M., Dunham, D. W., Palmer, D. M., et al. 2003a, *Earth Moon and Planets*, 93, 145
- Cudnik, B. M., Palmer, D. W., Palmer, D. M., et al. 2003b, *Earth Moon and Planets*, 93, 97
- Davis, S. S. 2009, *Icarus*, 202, 383
- Ernst, C. M., Barnouin, O. S., & Schultz, P. H. 2011, in *EPSC-DPS Joint Meeting 2011*, Vol. 2011, 1484
- Ernst, C. M. & Schultz, P. H. 2003, in *Lunar and Planetary Science Conference, Lunar and Planetary Science Conference, 2020*
- Ferrari, F., Pena Asensio, E., Sughì, S., et al. 2025, in *EPSC-DPS Joint Meeting 2025*, Vol. 2025, EPSC-DPS2025-1514
- Foreman-Mackey, D., Hogg, D. W., Lang, D., & Goodman, J. 2013, *PASP*, 125, 306
- Fuse, R., Abe, S., Yanagisawa, M., & Hasegawa, S. 2020, *Planet. Space Sci.*, 187, 104921
- Gores, P. A. S. & Spray, J. G. 2022, *International Journal of Impact Engineering*, 160, 104078
- Kolovos, G., Seiradakis, J. H., Varvoglis, H., & Avgoloupis, S. 1988, *Icarus*, 76, 525
- Liakos, A., Bonanos, A. Z., Xilouris, E. M., et al. 2020, *A&A*, 633, A112
- Liakos, A., Bonanos, A. Z., Xilouris, E. M., et al. 2024, *A&A*, 687, A14
- Madiedo, J. M., Ortiz, J. L., & Morales, N. 2018, *MNRAS*, 480, 5010
- Madiedo, J. M., Ortiz, J. L., Morales, N., & Cabrera-Cañó, J. 2015a, *Planet. Space Sci.*, 111, 105
- Madiedo, J. M., Ortiz, J. L., Morales, N., & Santos-Sanz, P. 2019, *MNRAS*, 486, 3380
- Madiedo, J. M., Ortiz, J. L., Organero, F., et al. 2015b, *A&A*, 577, A118
- Nelson, D. M., Koeber, S. D., Daud, K., et al. 2014, in *45th Annual Lunar and Planetary Science Conference, Lunar and Planetary Science Conference, 2861*
- Nemtchinov, I. V., Shuvalov, V. V., Artem’eva, N. A., et al. 1998, *Solar System Research*, 32, 99
- Ortiz, J. L., Aceituno, F. J., Quesada, J. A., et al. 2006, *Icarus*, 184, 319
- Ortiz, J. L., Madiedo, J. M., Morales, N., Santos-Sanz, P., & Aceituno, F. J. 2015, *MNRAS*, 454, 344
- Ortiz, J. L., Quesada, J. A., Aceituno, J., Aceituno, F. J., & Bellot Rubio, L. R. 2002, *ApJ*, 576, 567
- Ortiz, J. L., Sada, P. V., Bellot Rubio, L. R., et al. 2000, *Nature*, 405, 921
- Osinski, G. R., Silber, E. A., Clayton, J., et al. 2019, *Meteoritics & Planetary Science*, 54, 573
- Rakesh Chandra, N. 2026, *Ap&SS*, 371, 32
- Scott, D. W. 2015
- Sheward, D., Delbo, M., Avdellidou, C., et al. 2024, *MNRAS*, 529, 3828
- Song, D., Cai, H.-b., Wang, S., & Wang, J. 2025, *Advances in Space Research*, 75, 4061
- Spray, J. G. & Gores, P. 2019, in *LPI Contributions, Vol. 2136, Large Meteorite Impacts and Planetary Evolution VI*, ed. LPI Editorial Board, 5078
- Suggs, R. M., Cooke, W. J., Suggs, R. J., Swift, W. R., & Hollon, N. 2008, *Earth Moon and Planets*, 102, 293
- Suggs, R. M., Moser, D. E., Cooke, W. J., & Suggs, R. J. 2014, *Icarus*, 238, 23
- Swift, W. R., Moser, D. E., Suggs, R. M., & Cooke, W. J. 2011, in *Meteoroids: The Smallest Solar System Bodies*, ed. W. J. Cooke, D. E. Moser, B. F. Hardin, & D. Janches, 125
- Tandy, J. D., Price, M. C., Wozniakiewicz, P. J., et al. 2020, *Meteoritics & Planetary Science*, 55, 2301
- Virtanen, P., Gommers, R., Oliphant, T. E., et al. 2020, *Nature methods*, 17, 261
- Wagner, R., Speyerer, E., Robinson, M., team, L., et al. 2015, in *46th annual lunar and planetary science conference No. 1832*, 1473
- Xilouris, E. M., Bonanos, A. Z., Bellas-Velidis, I., et al. 2018, *A&A*, 619, A141
- Yanagisawa, M. & Kisaichi, N. 2002, *Icarus*, 159, 31
- Yanagisawa, M., Ohnishi, K., Takamura, Y., et al. 2006, *Icarus*, 182, 489
- Yanagisawa, M., Uchida, Y., Kurihara, S., et al. 2025, *Icarus*, 434, 116480
- Yanagisawa, M., Uchida, Y., Kurihara, S., et al. 2021, *Planet. Space Sci.*, 195, 105131

Appendix A: Additional figures and tables

Table A.1: New LIFs observed by NELIOTA between August 2025 and February 2026.

ID	Valid.	Dur. (ms)	Date & Time (UT)	$m_{R,peak}$ (mag)	$m_{I,peak}$ (mag)	Lat. (°)	Long. (°)	Source
296	V	66	2025-08-17 00:28:47.619	10.2 ± 0.3	9.24 ± 0.11	-7.9 ± 0.5	54.6 ± 0.5	SPO
297	SC1	66	2025-08-17 00:36:58.774		8.62 ± 0.09	46.0 ± 0.5	12.8 ± 0.5	SPO
298	SC1	66	2025-08-17 02:14:55.185		9.33 ± 0.10	-13.7 ± 0.5	71.6 ± 0.5	SPO
299	SC1	66	2025-08-20 02:24:15.476		9.20 ± 0.08	32.6 ± 0.5	-12.4 ± 0.5	SPO
300	SC2	33	2025-08-20 02:24:15.476		10.02 ± 0.12	51.9 ± 0.5	15.9 ± 0.5	SPO
301	V	132	2025-09-14 23:56:16.151	8.40 ± 0.13	7.63 ± 0.07	6 ± 1	72 ± 1	SPO
302	SC1	66	2025-09-15 01:03:26.148		9.00 ± 0.10	-18 ± 1	62 ± 1	SPO
303	SC2	33	2025-09-16 02:27:13.313		10.20 ± 0.24	-37 ± 1	85 ± 1	SPO
304	SC2	33	2025-09-17 02:58:25.604		9.52 ± 0.09	19 ± 1	68 ± 1	SPO
305	SC1	66	2025-10-28 16:31:32.388		8.5 ± 0.09	18 ± 1	-83 ± 1	SPO
306	SC2	33	2025-10-28 16:46:51.240		9.7 ± 0.4	6 ± 1	-29 ± 1	ORI
307	V	33	2025-10-28 18:32:01.270	7.58 ± 0.11	6.33 ± 0.09	-18 ± 1	-18 ± 1	ORI
308	SC1*	33	2025-11-13 02:10:02.383	8.77 ± 0.16	8.70 ± 0.13	-27 ± 1	21 ± 1	SPO
309	V	66	2025-11-13 02:21:24.302	10.9 ± 0.5	8.81 ± 0.09	9 ± 1	70 ± 1	SPO
310	V	99	2025-11-13 03:10:06.033	10.04 ± 0.24	8.47 ± 0.07	-5 ± 1	44 ± 1	SPO
311	V	33	2025-11-16 03:49:15.986	11.20 ± 0.29	10.03 ± 0.13	2.5 ± 0.5	12.5 ± 0.5	SPO
312	SC2	33	2025-11-16 03:55:52.917		9.54 ± 0.11	9.4 ± 0.5	38.0 ± 0.5	SPO
313	V	66	2025-11-16 04:27:15.941	10.7 ± 0.5	9.49 ± 0.24	19.5 ± 0.5	50.8 ± 0.5	SPO
314	SC1	66	2025-11-24 16:41:24.558		9.77 ± 0.14	22.9 ± 0.5	-28.8 ± 0.5	SPO
315	SC2	33	2025-12-13 04:26:10.455		8.96 ± 0.09	14 ± 1	37 ± 1	GEM
316	SC2	33	2025-12-14 02:25:35.027		10.31 ± 0.17	13 ± 1	82 ± 1	GEM
317	V	99	2025-12-14 02:32:34.360	9.59 ± 0.19	8.08 ± 0.09	-14 ± 1	42 ± 1	GEM
318	V	66	2025-12-14 02:45:18.590	9.21 ± 0.14	8.15 ± 0.08	-24 ± 1	63 ± 1	GEM
319	V	33	2025-12-14 02:52:05.254	10.13 ± 0.29	8.88 ± 0.09	12 ± 1	77 ± 1	GEM
320	SC2	33	2025-12-15 03:42:53.126		9.94 ± 0.16	3.5 ± 0.5	20.8 ± 0.5	GEM
321	V	99	2025-12-15 03:51:33.930	10.7 ± 0.3	8.8 ± 0.09	-22.0 ± 0.5	12.5 ± 0.5	GEM
322	SC2	33	2025-12-15 04:16:54.026		10.05 ± 0.12	16.2 ± 0.5	68.4 ± 0.5	GEM
323	V	99	2025-12-15 04:33:42.042	9.24 ± 0.10	7.99 ± 0.06	19.1 ± 0.5	58.2 ± 0.5	GEM
324	SC2	33	2025-12-15 04:47:50.551		10.16 ± 0.13	-3.8 ± 0.5	65.9 ± 0.5	GEM
325	V	66	2026-01-13 04:09:55.147	9.16 ± 0.11	8.42 ± 0.08	-42.8 ± 0.5	48.4 ± 0.5	SPO
326	V	66	2026-02-21 17:31:42.570	9.03 ± 0.13	8.31 ± 0.07	-34 ± 1	-1 ± 1	SPO
327	SC2	33	2026-02-23 16:59:19.400		7.76 ± 0.08	-12 ± 1	-11 ± 1	SPO
328	V	99	2026-02-23 17:58:19.746	9.6 ± 0.8	7.21 ± 0.05	15 ± 1	-18 ± 1	SPO
329	SC1	66	2026-02-23 19:52:19.732		8.76 ± 0.11	-20 ± 1	-29 ± 1	SPO

Notes. The ID numbers continue from the previous NELIOTA study by Liakos et al. (2024). V = Validated LIF; SC1/2 = Suspected LIF of Class 1/2 (see Liakos et al. 2024, for details); (*) denotes an abnormal $R-I$ index. The association of LIFs with active meteoroid streams was determined using the methods of Madiedo et al. (2015a,b) and Ortiz et al. (2015).

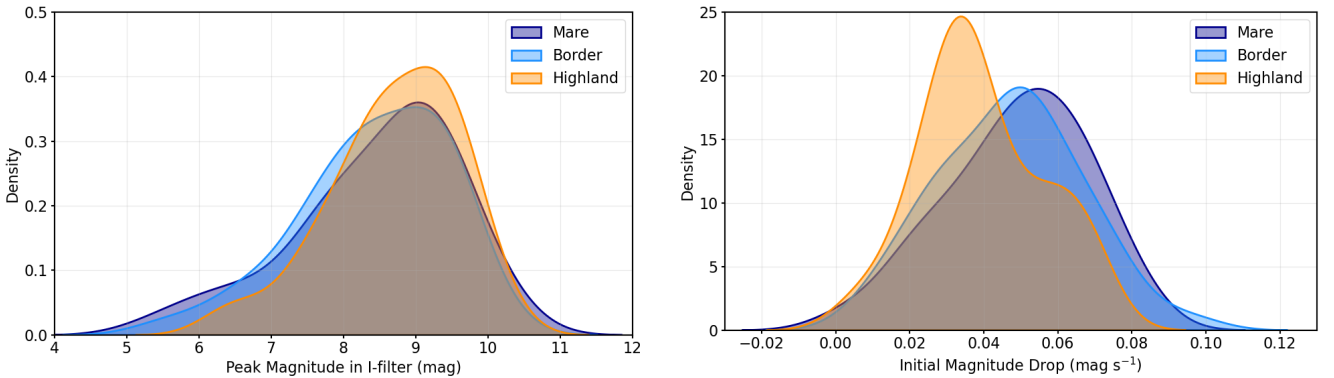


Fig. A.1: Kernel Density Estimation (KDE) of the peak magnitude in the I-filter (left) and of the initial magnitude drop (right). For the KDE, a Gaussian kernel was applied using SciPy (Virtanen et al. 2020), with the bandwidth determined according to Scott's rule (Scott 2015).

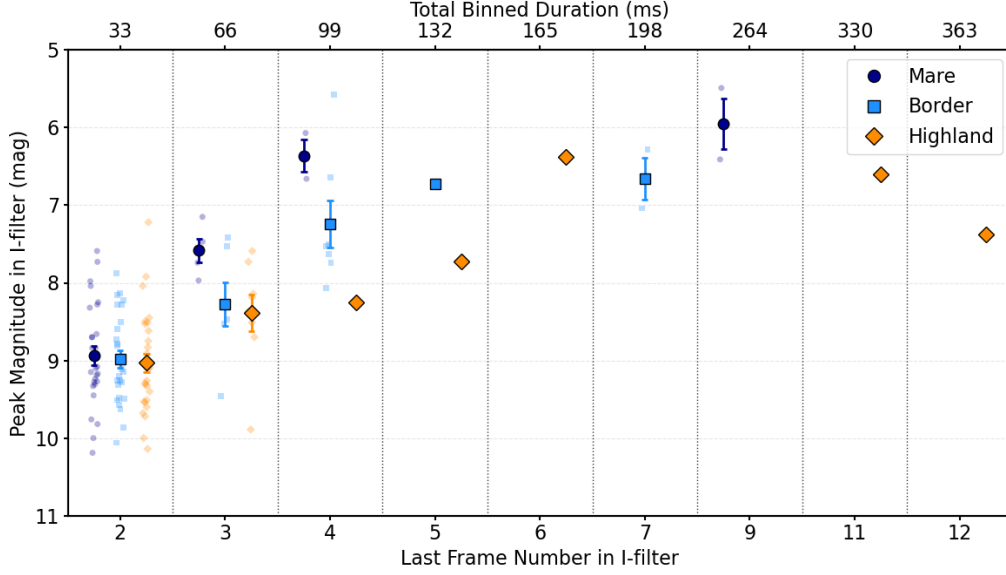


Fig. A.2: Peak magnitude of the multi-frame LIFs in the *I*-filter as a function of their duration (in bins of 33 ms) and the last frame in which they were detected. Different colours correspond to different terrain types. Individual measurements are shown with faded markers, while bold markers represent their average within each bin. Frame 2 corresponds to the first measurement following the peak, whereas the undisplayed Frame 1 represents the measurement captured at the peak.

Table A.2: Photometry of multi-frame sporadic LIFs observed by NELIOTA between August 2025 and February 2026.

ID	Frame	m_R (mag)	m_I (mag)	ID	Frame	m_R (mag)	m_I (mag)
296	i	10.2 ± 0.3	9.24 ± 0.1	310	i	10.04 ± 0.24	8.47 ± 0.07
	ii		10.38 ± 0.25		ii		8.75 ± 0.07
297	i	8.62 ± 0.09	8.62 ± 0.09		iii		10.3 ± 0.4
	ii		9.72 ± 0.22	313	i	10.7 ± 0.5	9.49 ± 0.24
298	i	9.33 ± 0.10	9.33 ± 0.10		ii		11.1 ± 0.4
	ii		10.63 ± 0.28	314	i	9.77 ± 0.14	9.77 ± 0.14
299	i	9.20 ± 0.08	9.20 ± 0.08		ii		11.1 ± 0.4
	ii		9.87 ± 0.12	325	i	9.16 ± 0.11	8.42 ± 0.08
301	i	8.40 ± 0.12	10.34 ± 0.26		ii		10.8 ± 0.4
	ii		7.63 ± 0.07	326	i	9.03 ± 0.13	8.31 ± 0.07
	iii		9.32 ± 0.11		ii		10.2 ± 0.3
	iv		10.16 ± 0.18		328		i
	v		11.40 ± 0.53	ii		7.93 ± 0.06	
302	i	9.00 ± 0.10	9.00 ± 0.10	iii	10.0 ± 0.4		
	ii		10.8 ± 0.4	329	i	8.76 ± 0.11	8.76 ± 0.11
305	i	8.50 ± 0.09	8.50 ± 0.09		ii		9.66 ± 0.25
	ii		10.29 ± 0.29				
309	i	10.9 ± 0.5	8.81 ± 0.09				
	ii		12 ± 1				

Table A.3: Distribution of NELIOTA multi-frame sporadic LIFs vs terrain type.

Terrain	Multi-frame	Pre-peak	Long
Mare	35 (31)	2 (2)	4 (4)
Border	42 (34)	1 (1)	10 (9)
Highland	42 (32)	4 (3)	5 (5)
Total	124 (97)	7 (6)	19 (18)

Notes. Numbers in parentheses correspond to the validated LIFs (those detected in both the *I* and *R* filters). ‘Pre-peak’ refers to LIFs with measurements prior to the peak magnitude in the *I*-filter, while ‘long’ refers to those with a duration longer than 100 ms. The multi-frame LIF data were adopted from Tables D.1 in Liakos et al. (2020), B.1 in Liakos et al. (2024), and A.2 of this work.

Table A.4: Terrain classification of multi-frame sporadic LIFs.

ID	Valid.	Terrain type	Mare Coverage (%)	ID	Valid.	Terrain type	Mare Coverage (%)	ID	Valid.	Terrain type	Mare Coverage (%)	ID	Valid.	Terrain type	Mare Coverage (%)
2	Yes	Mare	99	93	Yes	Highland	0	170	No	Border	93	259	Yes	Highland	0
6	Yes	Mare	99	94	Yes	Mare	100	171	Yes	Mare	100	261	Yes	Highland	0
9	No	Highland	0	95	Yes	Highland	0	172	Yes	Border	96	264	Yes	Mare	98
12	Yes	Mare	100	96	Yes	Border	16	173	No	Border	10	266	Yes	Highland	0
13	Yes	Border	44	97	Yes	Mare	100	177	Yes	Mare	100	267	Yes	Highland	0
14	Yes	Mare	100	100	Yes	Highland	0	180	Yes	Mare	99	269	Yes	Highland	0
20	Yes	Highland	0	107	Yes	Highland	0	182	Yes	Mare	100	270	No	Mare	100
21	Yes	Border	82	108	Yes	Mare	100	184	Yes	Highland	0	272	Yes	Border	77
22	Yes	Mare	100	118	Yes	Highland	0	185	Yes	Mare	100	279	Yes	Border	88
23	Yes	Border	61	124	Yes	Highland	0	186	Yes	Highland	0	280	Yes	Border	81
24	Yes	Highland	0	125	Yes	Border	90	187	No	Highland	0	281	Yes	Mare	100
26	Yes	Border	10	126	Yes	Border	47	188	Yes	Mare	100	282	Yes	Border	81
27	Yes	Border	57	127	Yes	Border	36	191	Yes	Border	6	283	Yes	Border	22
28	Yes	Highland	0	129	No	Border	62	195	Yes	Border	94	284	Yes	Border	97
29	Yes	Highland	0	130	Yes	Highland	0	196	No	Mare	100	287	Yes	Border	36
30	Yes	Border	75	133	No	Border	73	198	No	Highland	0	289	Yes	Border	46
32	Yes	Highland	0	136	Yes	Highland	0	199	Yes	Mare	100	291	No	Mare	100
33	Yes	Border	60	138	No	Border	71	202	Yes	Highland	0	296	Yes	Mare	100
35	No	Highland	0	142	Yes	Mare	100	204	Yes	Border	10	297	No	Highland	0
47	Yes	Border	20	144	Yes	Mare	100	205	Yes	Highland	0	298	No	Highland	0
58	Yes	Highland	0	145	Yes	Highland	0	206	Yes	Border	53	301	Yes	Border	42
59	Yes	Highland	0	148	Yes	Border	70	217	No	Highland	0	302	No	Border	44
61	Yes	Mare	100	150	No	Highland	0	219	Yes	Mare	100	305	No	Highland	0
62	Yes	Border	49	151	Yes	Mare	100	223	Yes	Border	62	309	Yes	Border	28
73	Yes	Highland	0	152	Yes	Mare	100	224	Yes	Highland	0	310	No	Border	85
74	Yes	Highland	0	153	Yes	Border	52	226	Yes	Border	88	313	Yes	Border	7
76	Yes	Border	7	160	Yes	Mare	100	227	No	Border	39	314	No	Border	11
78	Yes	Mare	100	162	Yes	Mare	100	235	Yes	Highland	0	325	Yes	Highland	0
80	No	Mare	100	163	Yes	Highland	0	252	Yes	Highland	0	326	Yes	Highland	0
85	Yes	Mare	100	168	Yes	Mare	100	253	No	Highland	0	328	Yes	Border	91
90	Yes	Highland	0	169	Yes	Mare	100	257	Yes	Mare	100	329	Yes	Border	-

Notes. The LIFs with IDs from 2 to 108 are reported in Liakos et al. (2020) and from 118 to 291 in Liakos et al. (2024). Mare coverage represents the percentage of the LIF area (defined by its localisation position and uncertainty) that overlaps with the mare region as defined by Nelson et al. (2014).

Appendix B: LIF cooling models

Laboratory experiments have shown that impacts are accompanied by the initial stages of impact crater formation; the contact and compression stage, and the excavation stage (Gores & Spray 2022). During the contact and compression stage, a vapour cloud or even plasma is produced, emitting radiation with a duration of less than 1 ms, as predicted by physical and numerical models (e.g., Nemtchinov et al. 1998; Artem'eva et al. 2001; Davis 2009). Various laboratory experiments have demonstrated this short timescale on lunar-analogue materials (e.g., Ernst & Schultz 2003; Spray & Gores 2019; Ernst et al. 2011; Tandy et al. 2020; Gores & Spray 2022). The emitted radiation during the second stage originates from the ejecta material, which cools down, causing a flash duration between 10 ms and ≈ 1 s (Bouley et al. 2012). Yanagisawa & Kisaichi (2002) and Yanagisawa et al. (2025) have developed the only LIF cooling models, also known as ejecta cooling models. In this work, we adapt these models to our data by incorporating their wavelength dependence, using the mathematical formalism of Bouley et al. (2012) and Song et al. (2025).

B.1. The Single-Size Molten Droplet Model

Yanagisawa & Kisaichi (2002) assumed that as the vapour plume cools rapidly, small spherical droplets of a uniform size are formed and radiate as blackbodies. In a more general approach, we can model these droplets as greybodies. The thermal evolution of a spherical droplet can be described by the heat conduction equation:

$$\frac{\partial T}{\partial t} = \frac{k}{c_p \rho} \frac{1}{r^2} \frac{\partial}{\partial r} \left(r^2 \frac{\partial T}{\partial r} \right), \quad (\text{B.1})$$

with the boundary condition at the surface temperature T_s : $k \frac{\partial T}{\partial r} = -\epsilon \sigma T_s^4$, where k is the thermal conductivity, c_p is the specific heat capacity, ρ is the droplet density, ϵ is the emissivity ($0 \leq \epsilon \leq 1$), and σ is the Stefan-Boltzmann constant.

Assuming a uniform temperature distribution within a droplet of radius R_d , integrating Equation (B.1) over the droplet volume yields:

$$\frac{4}{3} \pi R_d^3 c_p \rho \frac{dT}{dt} = -4 \pi R_d^2 \epsilon \sigma T^4 \quad \Rightarrow \quad \frac{dT}{dt} = -\frac{3 \epsilon \sigma}{R_d c_p \rho} T^4, \quad (\text{B.2})$$

The analytical solution to this differential equation is:

$$T(t) = \frac{T_0}{\left(1 + \frac{9 \epsilon \sigma T_0^3}{R_d c_p \rho} (t - t_{\text{ref}})\right)^{1/3}} \quad \Rightarrow \quad T(t) = T_0 \left(1 + \frac{t - t_{\text{ref}}}{\tau}\right)^{-1/3}, \quad (\text{B.3})$$

where T_0 is the initial temperature of the droplet at the onset time ($t_{\text{ref}} \geq 0$) of the liquid phase, which may not necessarily coincide with the time of the absolute flux peak ($t_{\text{peak}} = 0$). For mathematical convenience, we can define the characteristic cooling timescale as $\tau = \frac{R_d c_p \rho}{9 \epsilon \sigma T_0^3}$ as Bouley et al. (2012).

The radiative flux of a greybody is described by Planck's law multiplied by the emissivity:

$$f(\lambda, T) = \epsilon(\lambda) \frac{2 \pi h c^2}{\lambda^5} \frac{1}{e^{\frac{hc}{\lambda k_B T}} - 1}, \quad (\text{B.4})$$

where λ is the wavelength, h is the Planck constant, c is the speed of light and k_B is the Boltzmann constant. Assuming the emissivity is independent of wavelength ($\epsilon(\lambda) = \epsilon$) and the optical filter has a uniform response over a bandwidth $\Delta \lambda$ at an effective wavelength λ_{eff} , the spectral radiance becomes:

$$f_{\lambda}(T) \approx \epsilon \frac{2 \pi h c^2}{\lambda_{\text{eff}}^5} \Delta \lambda \frac{1}{e^{\frac{hc}{\lambda_{\text{eff}} k_B T}} - 1} \stackrel{\text{B.3}}{\Rightarrow} f_{\lambda}(t) = \epsilon \frac{2 \pi h c^2}{\lambda_{\text{eff}}^5} \Delta \lambda \left[e^{\frac{hc}{\lambda_{\text{eff}} k_B T_0} \left(1 + \frac{t - t_{\text{ref}}}{\tau}\right)^{1/3}} - 1 \right]^{-1}. \quad (\text{B.5})$$

The total luminosity is described by $L_{\lambda}(t) = A_{\text{eff}} f_{\lambda}(t)$, where the effective emitting area (A_{eff}) of the ejecta can be estimated as $A_{\text{eff}} = \frac{3 V_{\text{ej}}}{R_d}$, with V_{ej} representing the total ejecta melt volume, which is related to the mass impact velocity of the projectile (see, e.g., Song et al. 2025, and references therein).

Combining these relations, the absolute observed flux as a function of time is:

$$F_{\lambda}(t) = \frac{L_{\lambda}(t)}{f \pi D^2} \quad \Rightarrow \quad F_{\lambda}(t) = \underbrace{\epsilon \frac{6 V_{\text{ej}} h c^2}{f D^2 R_d \lambda_{\text{eff}}^5}}_{F_{\lambda,0}} \underbrace{\Delta \lambda \left[e^{\frac{hc}{\lambda_{\text{eff}} k_B T_0} \left(1 + \frac{t - t_{\text{ref}}}{\tau}\right)^{1/3}} - 1 \right]^{-1}}_{\Phi(t)} \quad \Rightarrow \quad F_{\lambda}(t) = F_{\lambda,0} \cdot \Phi(t), \quad (\text{B.6})$$

where f is a geometric factor ($2 \leq f \leq 4$) depending on the radiation anisotropy (see, e.g., Bouley et al. 2012), and D is the distance between the Earth and the lunar surface.

To fit this theoretical framework on our data, which are normalised such that the absolute maximum of the initial flash is unity ($F_{\text{peak}} = 1$), we must isolate the thermodynamic cooling profile from the unknown physical parameters embedded in $F_{\lambda,0}$ (namely, volume, distance, and droplet radius).

By evaluating Eq. (B.6) exactly at the reference time t_0 , we obtain $F_\lambda(t_{\text{ref}}) = F_{\lambda,0} \cdot \Phi(t_{\text{ref}})$. Taking the ratio of the time-dependent flux to this reference flux perfectly cancels the term $F_{\lambda,0}$, yielding the dimensionless cooling shape:

$$\frac{F_\lambda(t)}{F_\lambda(t_{\text{ref}})} = \frac{\Phi(t)}{\Phi(t_{\text{ref}})}. \quad (\text{B.7})$$

To map this theoretical shape onto our normalised dataset, we scale it by an amplitude parameter F_{ref} , yielding the final fitting function:

$$F_{\text{norm}}(t) = F_{\text{ref}} \cdot \frac{\Phi(t)}{\Phi(t_{\text{ref}})} + C_{\text{bg}}, \quad (\text{B.8})$$

where $F_{\text{ref}} = \frac{F_\lambda(t_{\text{ref}})}{F_{\text{peak}}}$ represents the fractional amplitude ($0 \leq F_{\text{ref}} \leq 1$) of the data at the onset of the molten droplet phase. Additionally, C_{bg} is a bounded free parameter ($-0.05 \leq C_{\text{bg}} \leq 0.05$) representing a mathematical baseline offset intended to account for residual, non-zero instrumental noise. The shape of this normalised thermal tail depends entirely on F_{ref} , T_0 , and τ .

B.2. The Dual-Size Molten Droplet Model

Yanagisawa et al. (2025) suggested that two distinct particle populations are ejected during the excavation phase, both contributing to the LIF radiation. Initially, fine molten droplets form at temperatures near the vaporization point of lunar minerals, followed by the ejection of coarse particles at lower initial temperatures. Due to their larger volume-to-surface-area ratio, these coarse particles cool much more slowly, acting as the primary source of the flux tail, the so-called ‘afterglow’.

Following the same mathematical derivation as the single-size model, Eq. (B.8) is expanded to account for both the fine (f) and coarse (c) populations:

$$F_{\text{norm}}(t) = F_{\text{ref}} \cdot \frac{\Phi_f(t) + A_R \Phi_c(t)}{\Phi_f(t_{\text{ref}}) + A_R \Phi_c(t_{\text{ref}})} + C_{\text{bg}}, \quad (\text{B.9})$$

where A_R is the cross-sectional area ratio between the coarse and fine particles. This parameter is directly related to their total volume ratio via the expression $\frac{V_c}{V_f} = A_R \frac{R_c}{R_f}$. Physically, impact cratering kinematics dictate that the hotter fine droplets are ejected slightly earlier than the cooler coarse aggregates. However, both populations are assumed to start simultaneously at the observational reference time (t_{ref}), which may lead to a slight overestimation of T_c . This is negligible given our current resolution.

Appendix C: Markov Chain Monte Carlo (MCMC) model fitting

We applied a MCMC approach to the I -filter average LIF light curve, owing to its extended duration in comparison with the R -filter. In Eq. (2), the effective wavelength of the I Cousins filter was set to $\lambda_{\text{eff}} = 798$ nm (Bonanos et al. 2018). The parameter space was explored using the `emcee` Python package (Foreman-Mackey et al. 2013). For the single-size model, the chains were evolved using 128 walkers running for 10,000 steps, with the first 5,000 steps discarded as a burn-in period to ensure convergence. To account for higher dimensionality and parameter degeneracy of the dual-size model, these computational parameters (walkers, total steps, and burn-in) were increased fourfold. Strict hierarchical physical priors (e.g., $T_f > T_c + 100$ K and $\tau_f < \tau_c$) were applied to the dual-size model to prevent population inversion. The final parameter estimates and their asymmetric 1σ credible intervals were derived from the median (50th percentile) and the 16th and 84th percentiles of the marginalised posterior distributions, respectively.

Table C.1: MCMC results for the free parameters of each model.

Single-size model free parameters								
Region	t_{ref} (s)	F_{ref}	T_{ref} (K)	τ (s)	C_{bg}			
Mare	0.018 ^{+0.007} _{-0.006}	0.51 ^{+0.23} _{-0.12}	3000 ⁺¹⁰⁰⁰ ₋₇₀₀	0.038 ^{+0.032} _{-0.018}	0.001 ^{+0.024} _{-0.026}			
Border	0.018 ^{+0.007} _{-0.006}	0.48 ^{+0.21} _{-0.10}	3000 ⁺⁹⁰⁰ ₋₇₀₀	0.050 ^{+0.039} _{-0.023}	-0.004 ^{+0.031} _{-0.030}			
Highland	0.018 ^{+0.008} _{-0.006}	0.42 ^{+0.09} _{-0.05}	3100 ⁺⁹⁰⁰ ₋₈₀₀	0.11 ^{+0.08} _{-0.05}	0.008 ^{+0.063} _{-0.035}			
Dual-size model free parameters								
Region	t_{ref} (s)	F_{ref}	A_R	T_f (K)	T_c (K)	τ_f (s)	τ_c (s)	C_{bg}
Mare	0.020 ^{+0.007} _{-0.006}	0.56 ^{+0.22} _{-0.15}	0.4 ^{+0.4} _{-0.3}	3600 ⁺⁶⁰⁰ ₋₇₀₀	2200 ⁺⁶⁰⁰ ₋₅₀₀	0.025 ^{+0.014} _{-0.011}	0.5 ^{+0.3} _{-0.3}	-0.003 ^{+0.024} _{-0.026}
Border	0.019 ^{+0.007} _{-0.006}	0.55 ^{+0.22} _{-0.14}	0.5 ^{+0.4} _{-0.3}	3700 ⁺⁶⁰⁰ ₋₇₀₀	2300 ⁺⁶⁰⁰ ₋₅₀₀	0.030 ^{+0.012} _{-0.013}	0.5 ^{+0.3} _{-0.3}	-0.003 ^{+0.028} _{-0.028}
Highland	0.018 ^{+0.008} _{-0.006}	0.57 ^{+0.19} _{-0.14}	0.6 ^{+0.3} _{-0.3}	3700 ⁺⁵⁰⁰ ₋₇₀₀	2700 ⁺⁵⁰⁰ ₋₆₀₀	0.036 ^{+0.010} _{-0.013}	0.5 ^{+0.3} _{-0.3}	0.020 ^{+0.020} _{-0.035}